J. Fluid Mech. (1984), *vol.* 148, *pp.* 319–348
Printed in Great Britain

An experimental investigation of coherent substructures associated with turbulent spots in a laminar boundary layer

By ERIC C. ITSWEIRE AND CHARLES W. VAN ATTA

Department of Applied Mechanics and Engineering Sciences, and Scripps Institution of Oceanography, University of California, San Diego, La Jolla, CA 92093

(Received 1 December 1983 and in revised form 17 April 1984)

Longitudinal and transverse components of the velocity were simultaneously measured for various vertical locations at 20 off-centreline positions in turbulent spots artificially generated in a zero-pressure-gradient laminar boundary layer. Global ensemble-averaged velocity diagrams and vertical vorticity contours were computed in similarity coordinates $\xi = (x-x_0)/(U_\infty(t-t_0))$ and $\zeta = z/(U_\infty(t-t_0))$ for different heights $\eta = y/\delta^*$ above the plate. This global averaging technique inadequately describes the spot, which is not a single large vortex structure. A discriminative averaging technique was developed to construct a 'statistically most-probable' spot with sufficient resolution to include some of the largest substructures detected in visual studies. Four eddies were identified in vertical slices of the central region of the spot, while several rows appeared in the plan view. These features of the velocity and vorticity contours of the statistically most-probable spot exhibit similarities with structures observed in flow visualizations.

1. Introduction

During the past few years, refined flow-visualization techniques have provided evidence which suggests that turbulent boundary-layer flows might be controlled by large 'coherent structures'. Head & Bandyopadhyay (1981), Perry, Lim & Teh (1981) and Perry & Chong (1982) showed the existence of Reynolds-number-dependent hairpin vortices originating from the wall in turbulent boundary layers. Such structures also appear to be present in a transitional spot artificially generated by a spark or a small air jet (Gad-El-Hak, Blackwelder & Riley 1981). Such spots have the advantage of being controllable and fairly reproducible isolated events.

The concept of turbulent spots occurring randomly in space and time was first introduced by Emmons (1951) from observations of transitional laminar boundary-layer flow on a 'water table'. The generation, growth and interaction of such three-dimensional structures eventually produces a fully turbulent boundary layer. Schubauer & Klebanoff (1956) mapped the general shape of an artificial transitional spot and measured the propagation velocities of its boundaries. Ensemble-averaged velocity measurements by Wygnanski, Sokolov & Friedman (1976) and Cantwell, Coles & Dimotakis (1978) – hereinafter referred to as WSF and CCD respectively – show that, in the global-ensemble-average sense, the spot can be approximated by a large single vortex tube having an arrowhead shape. Measurements in an incipient spot (Wygnanski 1981*a*, *b*) suggest that the spot is composed of several hairpin vortices, raising the question of whether a larger spot contains more such vortices or if the initial vortices simply grow.

Leonard (1980, 1981) produced a numerical simulation of a turbulent spot using a three-dimensional vortex-filament description of the vorticity field. In this representation, the disturbance that generates the spot is a localized vorticity perturbation of a field of otherwise straight vortex tubes. The numerical results are somewhat limited, since the model can satisfactorily represent only the very early time development of a spot in regions not too close to the wall. It nevertheless appears to give a good representation of the young spot's growth.

The flow visualizations of turbulent spot structure, especially those of Matsui (1980) and Perry *et al.* (1981) suggested rather diverse possibilities for the configuration of vortex-like substructures seen in both planform and vertical cross-sectional views of spots. This motivated the present attempt to identify substructures from hot-wire measurements which could be compared with flow visualizations. Since the planform structure appeared to be the least understood and most controversial, emphasis was placed on mapping the simultaneous behaviour of the two horizontal velocity components in planes parallel to the wall using both global ensemble averaging (on the scale of the whole spot) and smaller-scale averaging aligned with the most prominent substructures detected by an objective criterion. Most of the hot-wire measurements to date involve the longitudinal (u) and vertical components (v) of the velocity in the plane of symmetry of turbulent spots (e.g. CCD; Antonia *et al.* 1981; Wygnanski, Zilberman & Haritonidis 1982). WSF reported some measurements of the transversal (w) velocity on and off the centreline, but a more extensive set of data with a small mesh size is required to characterize the horizontal structures of turbulent spots.

Another question of interest is the physical mechanism involved in the rapid lateral growth of turbulent spots. Several investigators (Gad-El-Hak *et al.* 1981; Wygnanski 1981*b*) suggested that the lateral addition of previously non-turbulent fluid into turbulent spots was not by direct contact or diffusion of vorticity (classical entrainment) but by destabilization of the unstable laminar boundary layer in the vicinity of the turbulent region. As evidence, Gad-El-Hak *et al.* (1981) injected blue dye from the solenoid valve generating the turbulent spots in order to tag the initial turbulent patch, while the background fluid was marked with red dye. They observed that new turbulent fluid (red dye) was added to the spot without mixing with initial turbulent fluid (blue dye).

Sections 2 and 3 present the experimental conditions and the measurements. In particular, the advantages and limitations of the Λ-probe versus a classical X-wire probe are discussed, as well as the calibration method used to separate u and w. An estimate of the velocity errors is also given. In §4 the results are presented in terms of globally ensemble-averaged data, and using the conical coordinates introduced by CCD. A global analysis does not provide detailed information on the smaller vortical structures of turbulent spots observed in flow visualizations, but is required for comparing some of the present data to earlier measurements by other investigators. Sections 5 and 6 describe a selective local averaging technique which provides a detailed representation of certain large substructures associated with turbulent spots which may be compared with visual observations. The conical similarity transformation in (x, z, t) is again employed to compute the vertical component of vorticity, allowing further comparisons with numerical simulations and flow visualizations. Velocity diagrams in three different horizontal planes show that the vortical structure of the wingtips of the spots (corresponding to new fluid added by destabilization) is different from the structure of the centreline region (initial turbulent fluid).

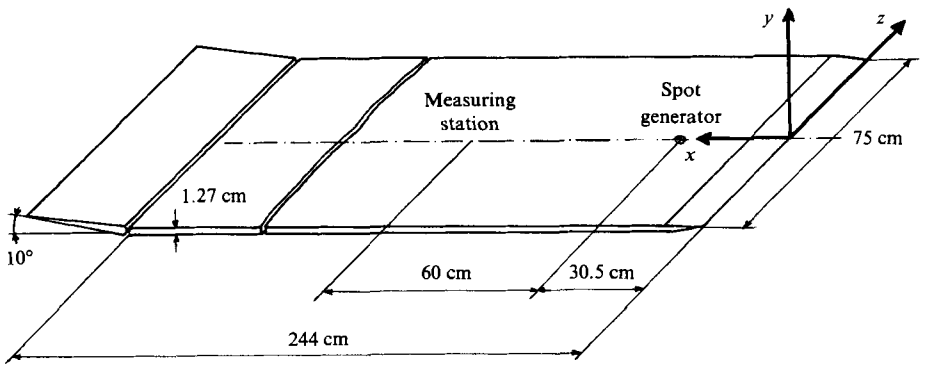

FIGURE 1. Perspective view of the plate and coordinate system.

2. Experimental set-up and apparatus

The measurements were made in the low-speed low-turbulence closed-loop wind tunnel in the Department of Applied Mechanics and Engineering Sciences at the University of California, San Diego. As described by Mautner & Van Atta (1982), the flat plate was mounted in the 76 cm × 76 cm cross-section test section, supported on adjustable jacks in a horizontal position at a height of 24 cm above the tunnel floor.

A 10 cm long leading edge consisting essentially of a 9° angle wedge was added to the 2.44 m long plate. The wedge extended 7.6 cm upstream of the constant-thickness section. All the joints were filled and the surface carefully hand polished with metal wax. All the holes used for the earlier shear-stress measurements of Mautner (1983) were plugged and the pressure taps closed.

The turbulent spots were artificially generated by a 5 cm diameter audio speaker mounted on the bottom of the plate. The speaker was driven by a 10 V pulse and created a small air jet through a 3.2 mm diameter hole in the plate at $x_s = 30.5$ cm from the leading edge. The pulse duration of 50 μs chosen was the shortest possible that generated a well-developed spot at the measuring station. Tests with several different pulse lengths suggested that the spot's duration increased with the pulse length, a result consistent with observations by WSF. A perspective view of the plate and the coordinate axes is shown in figure 1.

The pressure distribution along the length of the plate was adjusted using the technique described by Mautner & Van Atta (1982). A trailing-edge flap set at a 10° angle fixed the location of the stagnation point on the working surface and reduced transversal contamination from the leading edge by inducing a small air flow through the gap between the plate and the sidewalls of the wind tunnel. The static pressure at the plate surface was then measured at some of the pressure taps. The overall longitudinal pressure gradient was small, i.e. $dC_P/dx = -1.4 \times 10^{-4}$ cm^{-1} for $U_\infty = 8.6$ m/s, where $C_P = 2(P-P_\infty)/\rho U_\infty^2$.

The free-stream velocity was monitored by a Pitot tube connected to a 10 mmHg range pressure transducer. The mean vertical velocity profile measured at the station $x = 90.5$ cm for $U_\infty = 8.6$ m/s is compared with the theoretical Blasius profile in figure 2.

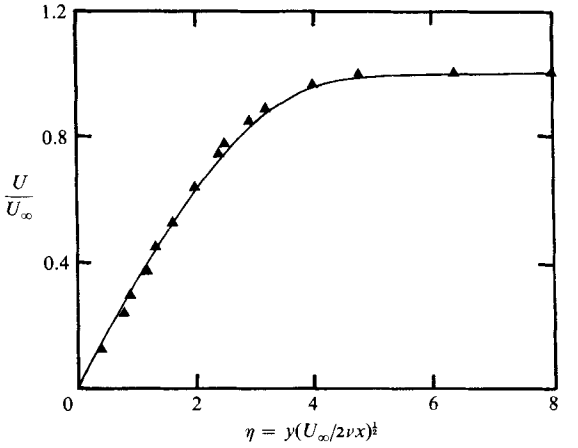

FIGURE 2. Measured and theoretical laminar boundary-layer velocity profiles.

3. Measurements and data acquisition

Simultaneous measurements of both longitudinal (u) and transversal (w) velocity components were taken at 12 vertical (y) and 20 transverse (z) locations at the downstream station $x = 90.5$ cm from the leading edge of the plate. A specially constructed small Λ-shaped probe was used to eliminate the effects of vertical velocity gradients associated with X-wire u-, w-measurements in the boundary layer. Platinum–Rhodium (10%) 5 μm diameter wires were soldered to the tips of four gold-plated needles at angles of approximately $\pm 40°$ with respect to the probe axis. The sensing length of the wires was 1 mm, which gave an overall probe width of 1.5 mm. The hot-wire signals from the two DISA 55M01 constant-temperature anemometers were passed through buck-and-gain amplifiers and low-pass filters before being digitized with a 14-bit resolution A/D converter at a sample rate of 7000 Hz. A square-wave generator triggered the pulse generator connected to the speaker. The pulses were fed to the DEC 11/23 microcomputer, where they were delayed by the data-acquisition software before triggering the A/D converter. The number of samples and the time delay were varied to optimize the data-acquisition process. A 65 ms delay was selected and 1000 samples were taken, except near the outer edge of the spot, where the delay was 80 ms and 800 samples were taken.

The Λ-wire probe was calibrated in the outer flow at seven different mean speeds by rotating the probe to pitch angles of 0°, $\pm 5°$, $\pm 10°$, $\pm 15°$ and $\pm 20°$. The wide range of pitch angles was necessary to cover the large range of fluctuations inside the turbulent spots. Nevertheless, strong velocity gradients, especially in the longitudinal ($\partial U/\partial x$) and vertical ($\partial U/\partial y$) directions, occur both at the leading edge and inside turbulent spots. They introduce errors in the velocity because of the finite length of the sensing wires of a Λ- or X-wire probe along the gradient direction.

WSF also used a Λ-shaped probe of comparable size to ours (the separation between the centres of the wires was less than 1 mm). They did not report any differences between longitudinal-velocity traces measured with single wires and their Λ-probe. Antonia *et al.* (1981) and Wygnanski *et al.* (1982) used X-wire probes to measure u and v and also did not discuss the effect of the probe resolution on the measured longitudinal velocity. A simplified model assuming a spatially uniform wire response may be used to evaluate the error introduced in the longitudinal velocity by velocity

gradients (see the Appendix). It yields the following expression for the error in velocity:

$$U_{\text{error}} = \frac{l}{8}\frac{\partial U}{\partial x},$$

where l is the sensing length of the wire in the direction of the gradient. In the present probe configuration $l = 0.7$ mm. If one assumes that the fluid particles near the leading edge move with the speed U_ℓ of the surrounding laminar fluid (the interface velocity of the leading edge is actually greater than $0.6U_\infty$ depending on the spanwise distance from the centreline), then

$$\frac{\partial U}{\partial x} \approx \frac{1}{U_\ell}\frac{\partial U}{\partial t}.$$

For the bottom traces of figure 4 ($y = 0.5$ mm, corresponding to the steepest gradient at the leading edge), the laminar velocity is

$$U_\ell = 0.1U_\infty.$$

Therefore

$$\frac{\partial U}{\partial x} \lesssim 400 \text{ s}^{-1},$$

which gives an estimated velocity error

$$U_{\text{error}} \lesssim 3.5 \text{ cm/s},$$

i.e. about 0.4 % of the free-stream velocity U_∞. With the spanwise gradients $\partial U/\partial z$ of the same order as the longitudinal gradients $\partial U/\partial x$, the total error in $\langle U \rangle$ due to the spatial resolution of the hot wires can be estimated to be

$$U_{\text{error}} \lesssim 7 \text{ cm/s} \quad \text{or} \quad 0.0081U_\infty.$$

The maximum peak-to-peak noise velocity measured from the averaged profiles of figure 4 is $0.0076U_\infty$, consistent with the estimate from our simple model. Since the transverse velocity w is obtained as a difference between the two hot-wire signals, one expects the error in w to be twice the error in u. The maximum peak-to-peak value measured from figure 5 is $0.015U_\infty$, again consistent with our estimate.

If one considers individual spots (see figure 12) instead of ensemble-averaged spots, the longitudinal-velocity gradients near the leading edge can be as much as four times larger. A good estimate for the velocity error introduced by the longitudinal gradient will be

$$U_{\text{error}} < 14 \text{ cm/s} \quad \text{or} \quad 0.016U_\infty.$$

A systematic error analysis of the cross-velocity calibrations was performed to test the linear fit of u, w in terms of both 'linearized' bridge voltages. A second-order regression including cross-products of the 'linearized' bridge voltages was tried, but no significant improvement in the cross-velocity calibration was observed. For computational efficiency a third-order polynomial fit was substituted for King's law.

4. Ensemble-mean velocity and vorticity

Ensemble-mean velocities $\langle U \rangle$ and $\langle W \rangle$ were computed by averaging over 250 realizations. Five vertical profiles of these averaged velocities are shown in figures 3 and 4 for off-axis locations $z = -1$, 2, 16, 34 and 57 mm, with traces aligned in time

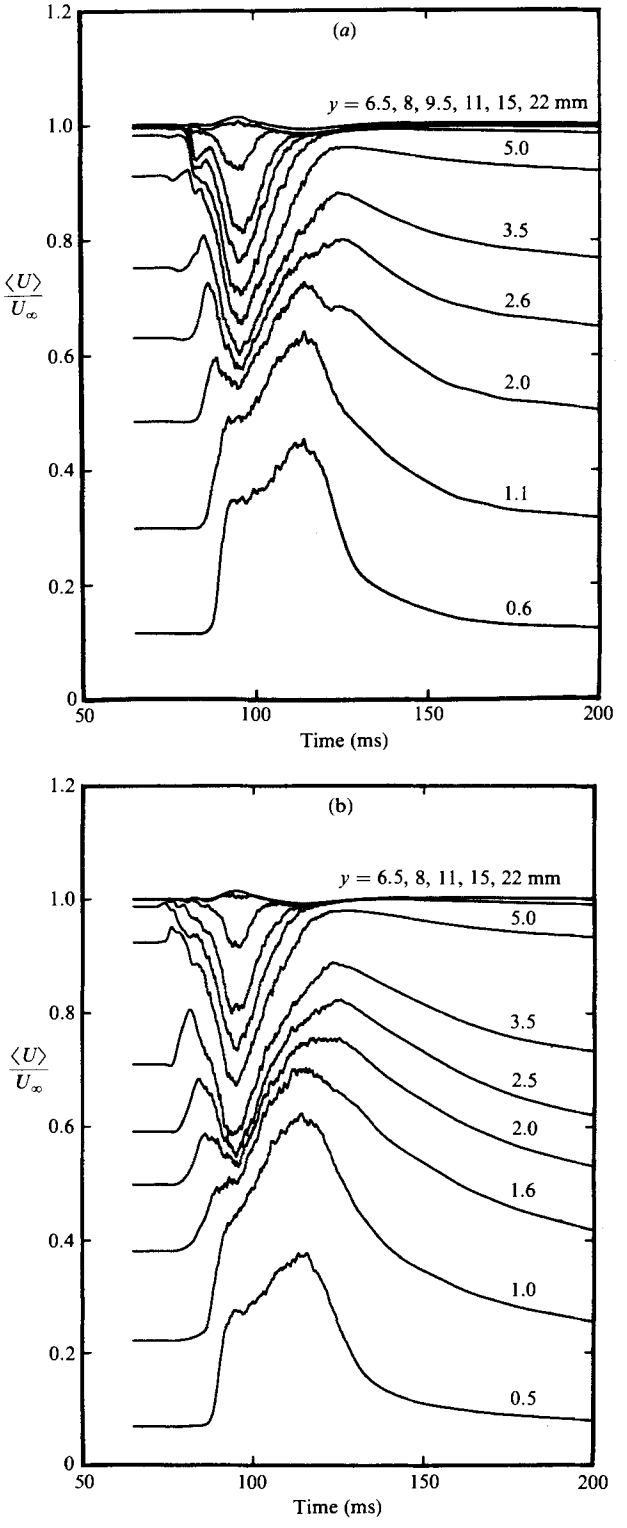

FIGURE 3(*a*, *b*). For caption see p. 326.

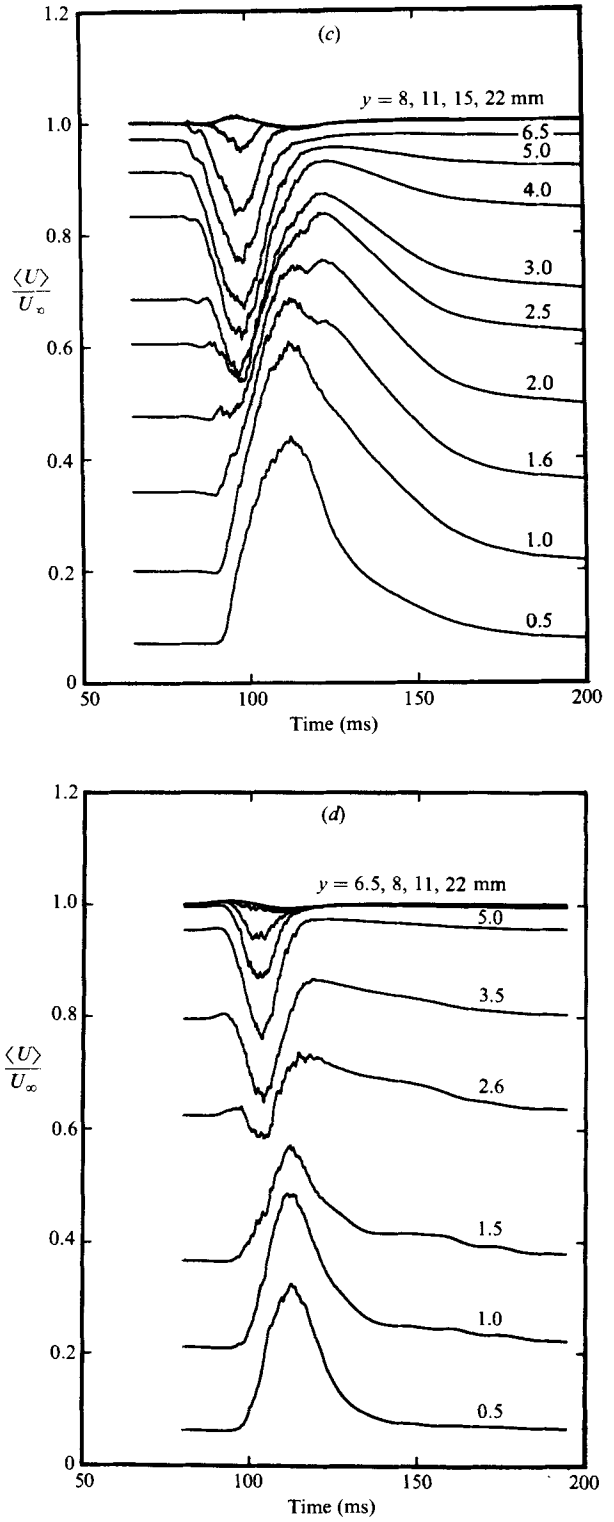

FIGURE 3(*c*, *d*). For caption see p. 326.

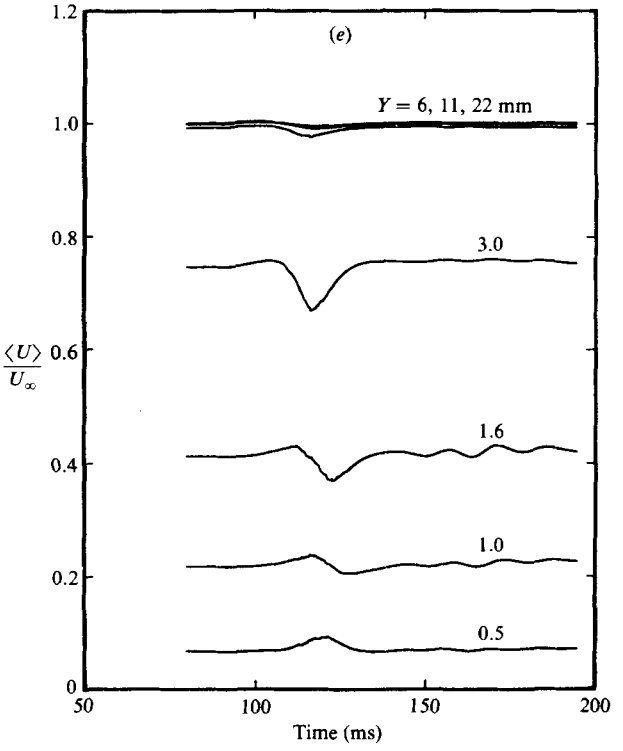

FIGURE 3. Vertical profiles of the ensemble-averaged longitudinal velocity $\langle U\rangle/U_\infty$ at (*a*) $z = -1$ mm; (*b*) 2 mm; (*c*) 16 mm; (*d*) 34 mm; (*e*) 57 mm.

with respect to the spot-generator pulse. Profiles for all the off-axis stations can be found in Itsweire (1983). The most widely accepted way to define the leading and trailing edges of the spot (e.g. WSF) is to locate the $\pm 2\%$ U_∞ perturbation velocity contours, where the perturbation velocity is defined as follows:

$$U_{\text{pert}} = \langle U\rangle - U_\ell,$$

where U_ℓ is the longitudinal velocity of the unperturbed laminar boundary layer at the current height. Alternatively, all the spots can be aligned on their leading edges before ensemble averaging, and the observed change is a sharper leading edge as found, for example, in Van Atta & Helland (1980). This alternative procedure for computing the ensemble-averaged velocity field is arguably sensible in that spots arriving early tend to be longer and stronger than those arriving at a later time. It can be noted that the return to the laminar value U_ℓ is slow and perfectly smooth (see figure 10). For $z \geqslant 34$ mm the Tollmien–Schlichting waves following the spots were first observed, as by Wygnanski, Haritonidis & Kaplan (1979), while for $z \geqslant 57$ mm the turbulent spots are very intermittent. Comparison between $\langle W\rangle/U_\infty$ on both sides of the centreline shows that the transverse ensemble-averaged velocity changes sign, in agreement with the assumption that spots are symmetrical relative to the centreline, at least in the ensemble-average sense. The instantaneous transversal velocity W of individual spots is non-zero on the centreline and can have a much larger amplitude than the ensemble-averaged value $\langle W\rangle$. It was observed that the averaged velocity traces of W are not as smooth as the $\langle U\rangle$ traces. The large differences in the amplitude of W between the ensemble-averaged spot and individual spots,

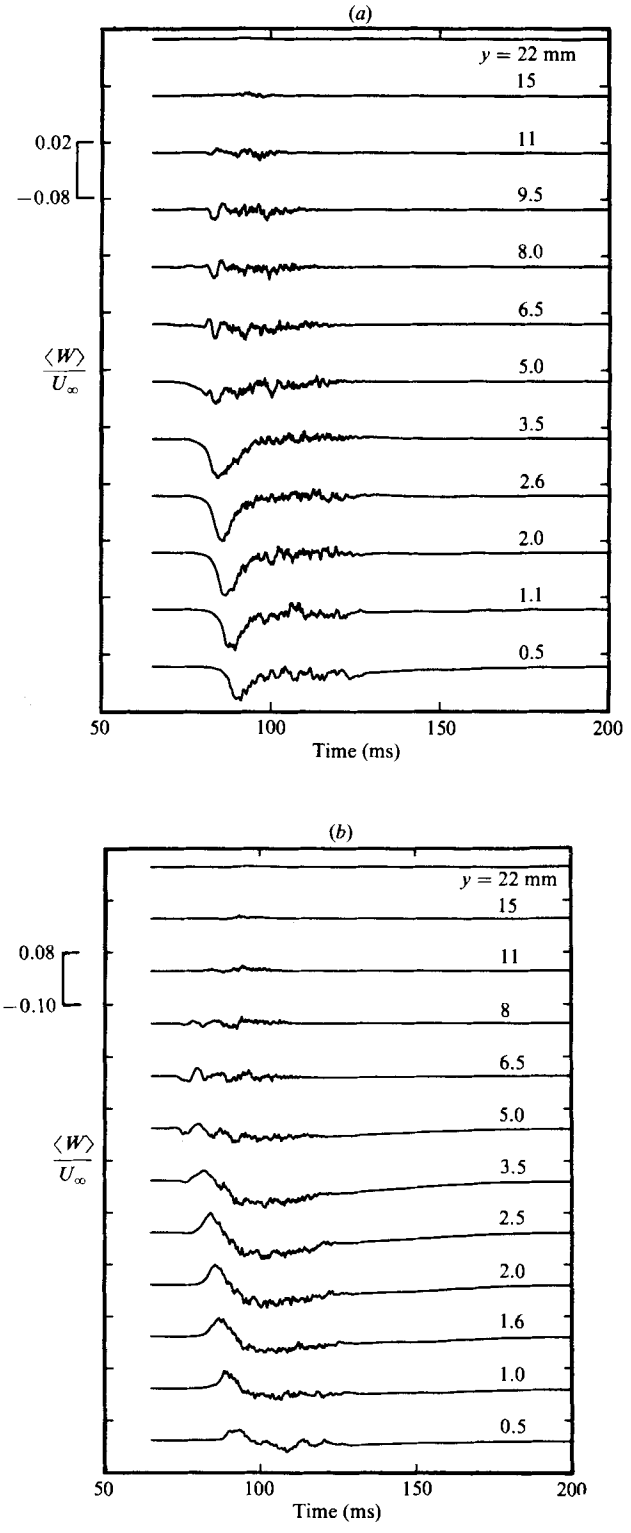

FIGURE 4(*a*, *b*). For caption see p. 329.

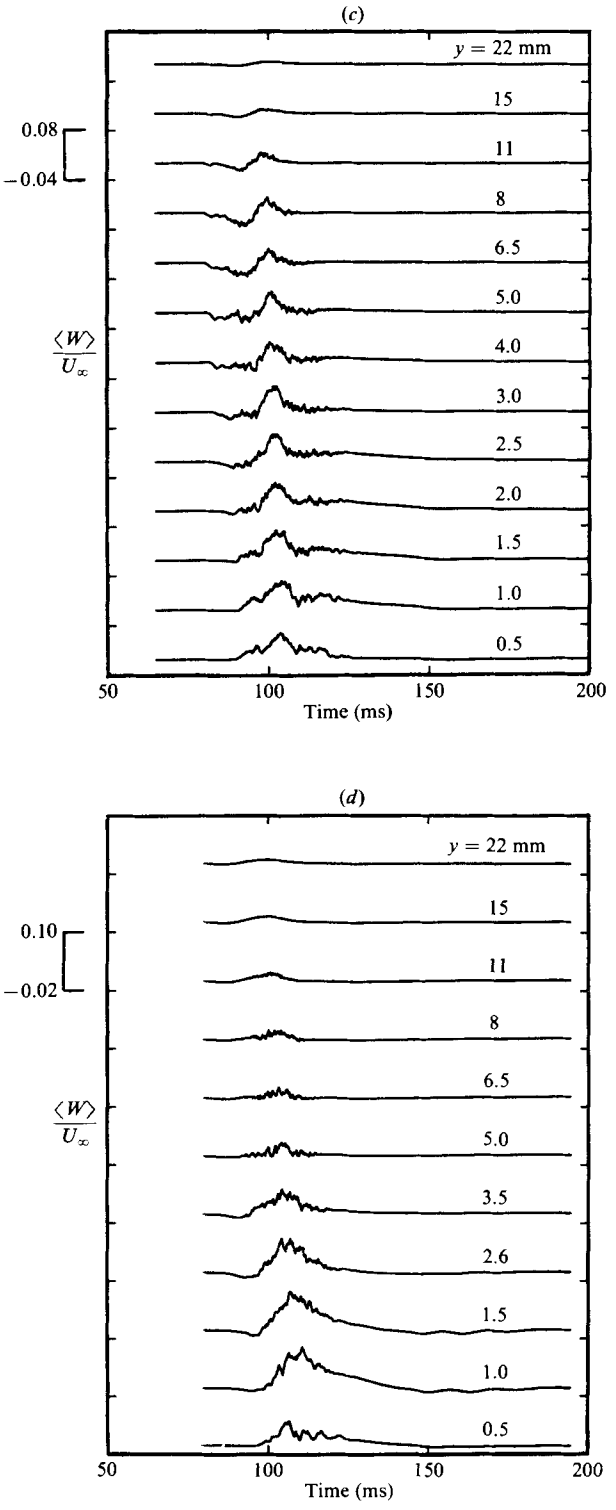

FIGURE 4(c, d). For caption see p. 329.

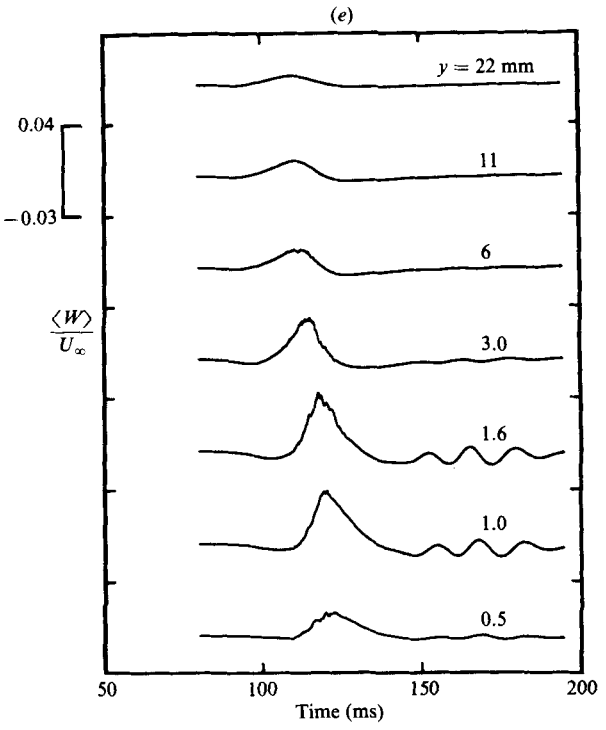

FIGURE 4. Vertical profiles of the ensemble-averaged transverse velocity $\langle W\rangle/U_\infty$ at (*a*) $z = -1$ mm; (*b*) 2 mm; (*c*) 16 mm; (*d*) 34 mm; (*e*) 57 mm.

combined with the jitter in arrival times mentioned earlier, create an apparent r.m.s. fluctuation. Ensemble averaging over a larger number of realizations might eliminate the high-frequency fluctuations observed in the measured $\langle W\rangle$.

Figures 5(*a*, *b*) show an elevation view of constant perturbation velocity $\langle U\rangle - U_\ell$ and $\langle W\rangle$ at $z = -1$ mm. The vertical coordinate was made non-dimensionless by the laminar boundary-layer thickness δ_ℓ, defined as the height where the velocity is $0.99U_\infty$ (e.g. Schlichting 1956):

$$\delta_\ell = 5.3\left(\frac{\nu x}{U_\infty}\right)^{\frac{1}{2}}.$$

In the present case the measured spot height is $h = 3\delta_\ell$. The plan view of figure 6 presents contours of constant $\langle U\rangle - U_\ell$ at a height of $y = 0.5$ mm. The measured half-width of the averaged spot was $b = 60$ mm. Both h and b are smaller than the values obtained by WSF because the spots were measured at a station closer to the spot generator. The definitions of h and b are somewhat arbitrary, since individual turbulent spots can have different sizes owing to a lack of reproducibility. In the present experiment, h and b are defined respectively as the maximum spot height and maximum spot width from the $\pm 2\,\%$ perturbation-velocity contours. This method tends to underestimate the dimensions of the average spot, as the weaker spots are not rejected when computing the ensemble-mean velocity. For example, Wygnanski (1981*a*) recomputed the ensemble average, rejecting all the spots for which the correlation coefficient between the instantaneous velocity U and the global ensemble mean $\langle U\rangle$ was less than 0.5.

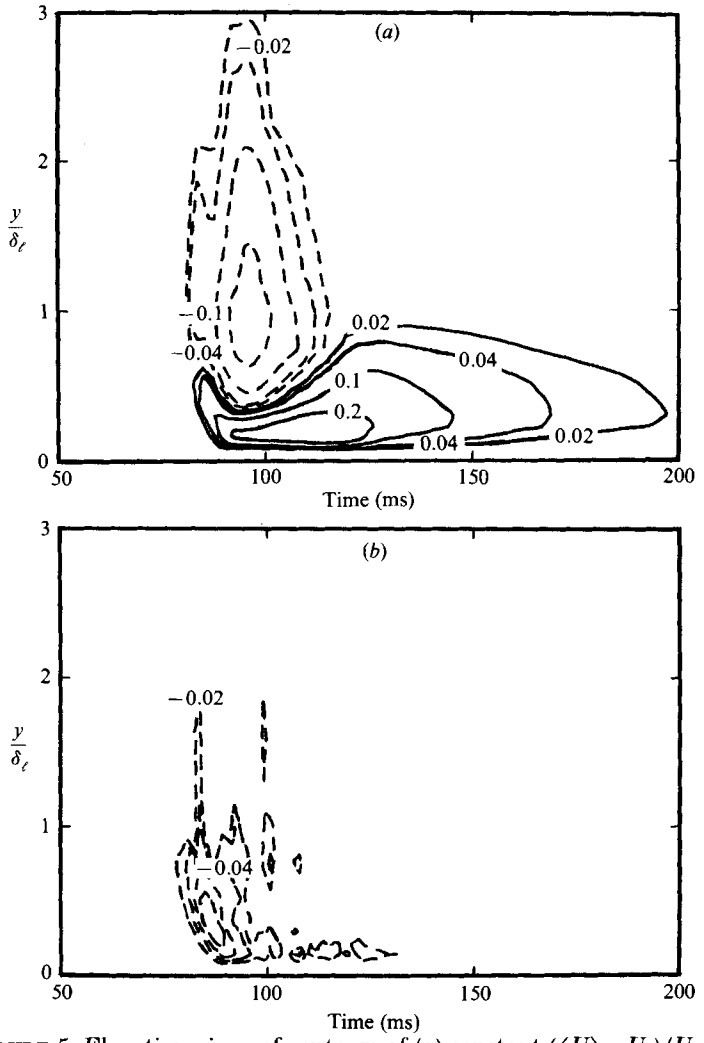

FIGURE 5. Elevation views of contours of (*a*) constant $(\langle U\rangle - U_\ell)/U_\infty$ and (*b*) constant $\langle W\rangle/U_\infty$ at $z = -1$ mm.

Cantwell *et al.* (1978) established that their ensemble-averaged spots were growing linearly in time and introduced similarity coordinates

$$\xi = \frac{x-x_0}{U_\infty(t-t_0)}, \quad \eta = \frac{y}{U_\infty(t-t_0)}, \quad \zeta = \frac{z}{U_\infty(t-t_0)},$$

where (x_0, t_0) is a virtual origin to be experimentally determined. Since the present measurements were made at only one downstream station, it was not possible to establish directly that the data satisfy the conical similarity transformation. Nevertheless, with the same experimental set-up, Mautner (1983) showed that the velocity field as well as the pressure field satisfy this transformation for measurements at three stations, the first of which was the one presently used. His free-stream velocity range included our velocity (7.8 and 10 m/s compared with 8.6 m/s). Wygnanski *et al.* (1982, their figure 15) also showed that with a free-stream velocity greater than 6 m/s the spanwise growth of the spot was linear for downstream distances from the spot generator larger than 40 cm. They found that the spanwise rate of growth was

y (mm)	ξ	ζ	z/b
0.50	0.69	0.035	0.765
2.5	0.72	0.035	0.733
5.0	0.74	0.035	0.713

TABLE 1. Loci of the maximum $\langle W \rangle$

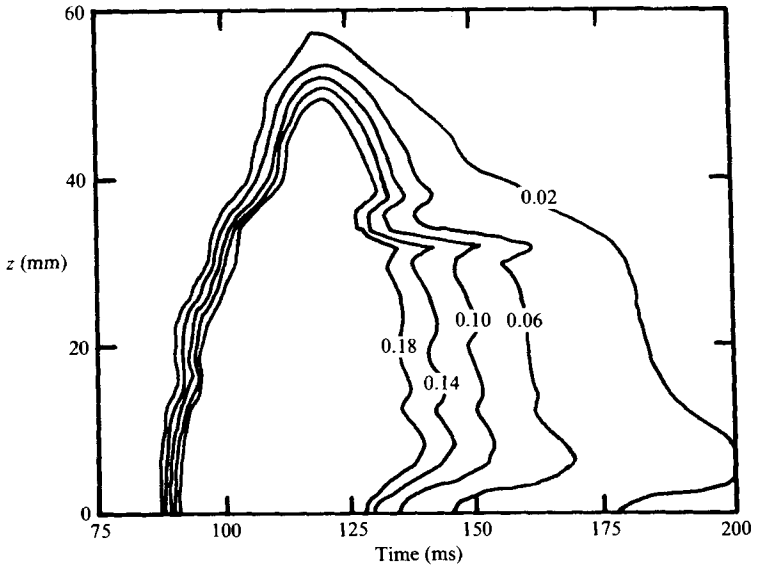

FIGURE 6. Plan view of contours of constant $(\langle U \rangle - U_\ell)/U_\infty$ at $y = 0.5$ mm.

independent of the Reynolds number at the spot generator and that only the virtual origins for the growth depended on the free-stream velocity. These findings and other observations justify the use of a conical transformation to describe the overall properties of turbulent spots in horizontal planes.

In the present experiment the virtual origins were $x_0 = 0$ and $t_0 = -35$ ms, as in Mautner (1983), who argues that virtual origins are non-universal, and depend on the experimental set-up, i.e. geometry of the plate leading edge and location of the spot generator from the leading edge.

In the following figures, measurements made for positive values of z were folded over using the symmetry of the ensemble-averaged spots with respect to the centreline. Perspective views of the longitudinal perturbation velocity at $y = 0.5$ mm, 2.5 mm and 5 mm show that the ensemble-averaged spots behave like a single large structure (figure 7). Except for the location closest to the wall ($y = 0.5$ mm), the central region of the spot seems to move at a nearly constant velocity $0.78U_\infty$. Such observations indicate the differences between the ensemble-averaged representation of turbulent spots and the visual observations of Gad-El-Hak *et al.* (1981) showing a very streaky structure in a plan view of an individual turbulent spot. The spanwise component of velocity $\langle W \rangle$ is essentially positive for $z > 0$, but has larger relative amplitude changes than $\langle U \rangle$. A maximum $\langle W \rangle$ is observed off-axis near the edge of the spot. Table 1 gives the location of this maximum excess velocity for the heights

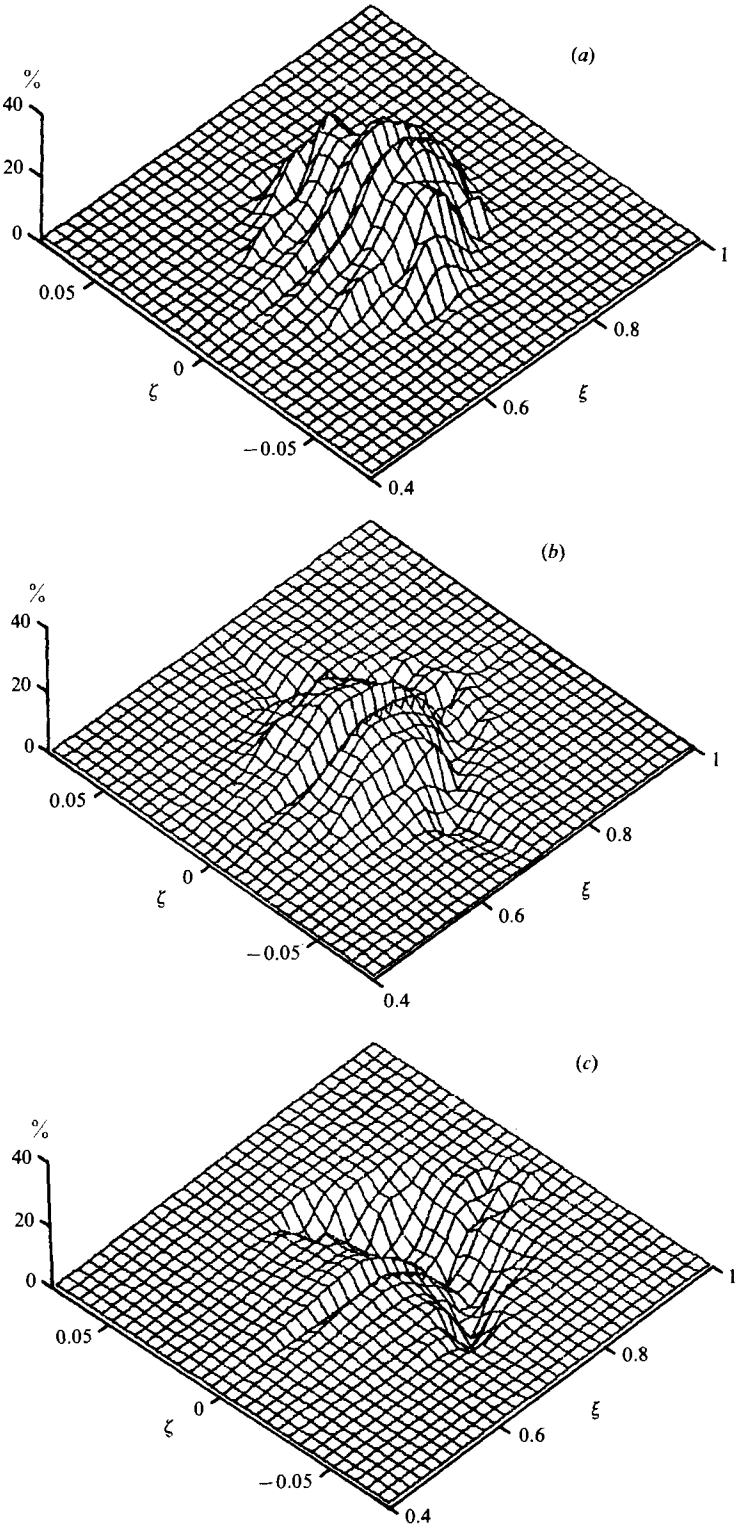

FIGURE 7. Perspective views of $(\langle U\rangle - U_\ell)/U_\infty$ in similarity coordinates at: (*a*) $y = 0.5$ mm; (*b*) 2.5 mm; (*c*) 5 mm.

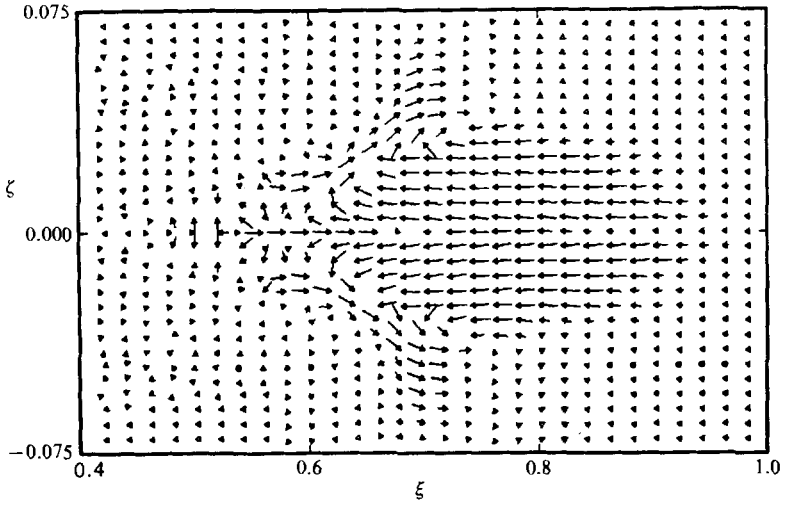

FIGURE 8. Ensemble-averaged velocity-vector diagrams in similarity coordinates at $y = 2.5$ mm.

considered. The average spanwise location of the maximum is $z/b = 0.74$. The temporal ensemble-averaged time series exhibit a maximum velocity $\langle W\rangle/U_\infty$ of 0.075 at $y/h = 0.125$ and $z/b = 0.717$, which may be compared with WSF's value of $\langle W\rangle/U_\infty \approx 0.07$ at $z/b = 0.7$. The vertical location of the WSF data is $y/h = 0.325$, and might not represent the height where the absolute maximum occurs.

The simultaneous measurements of U and W were combined to obtain ensemble-averaged velocity diagrams in horizontal planes. Each arrow in figure 8 points in the resultant horizontal flow direction and has a length proportional to the local velocity perturbation. The vector lower cut-off length is equal to half the maximum velocity perturbation in each horizontal plane. At $y = 2.5$ mm (figure 8) most of the new fluid seems to be added at the trailing edge of the wingtips of the spot. Since this layer of fluid is moving faster than the layer below it, the laminar fluid being destabilized along the side of the spot has to come from wall regions. The apparent stagnation point on the centreline at $\xi = 0.71$, $\eta = 0.002$ corresponds closely to the stagnation point identified as focus II at $\xi = 0.735$, $\eta = 0.0024$ in the centreline vertical cut of Cantwell *et al.* (1978) and Itsweire & Van Atta (1983).

The vertical component of vorticity Ω cannot be computed directly in the present case since all the measurements were taken at a fixed x-location in an unsteady flow. The use of the conical growth law for x and z makes it possible to define a dimensionless vertical vorticity ω as follows:

$$\Omega = \frac{1}{T}\omega(\xi, \eta', \zeta),$$

where $T = t - t_0$. The change of variables from $(x, z; t)$ to (ξ, ζ) gives

$$\frac{\partial U}{\partial z} = \frac{\partial U}{\partial \zeta}\frac{\partial \zeta}{\partial z} = \frac{1}{U_\infty(t-t_0)}\frac{\partial U}{\partial \zeta},$$

$$\frac{\partial W}{\partial x} = \frac{\partial W}{\partial \xi}\frac{\partial \xi}{\partial x} = \frac{1}{U_\infty(t-t_0)}\frac{\partial W}{\partial \xi},$$

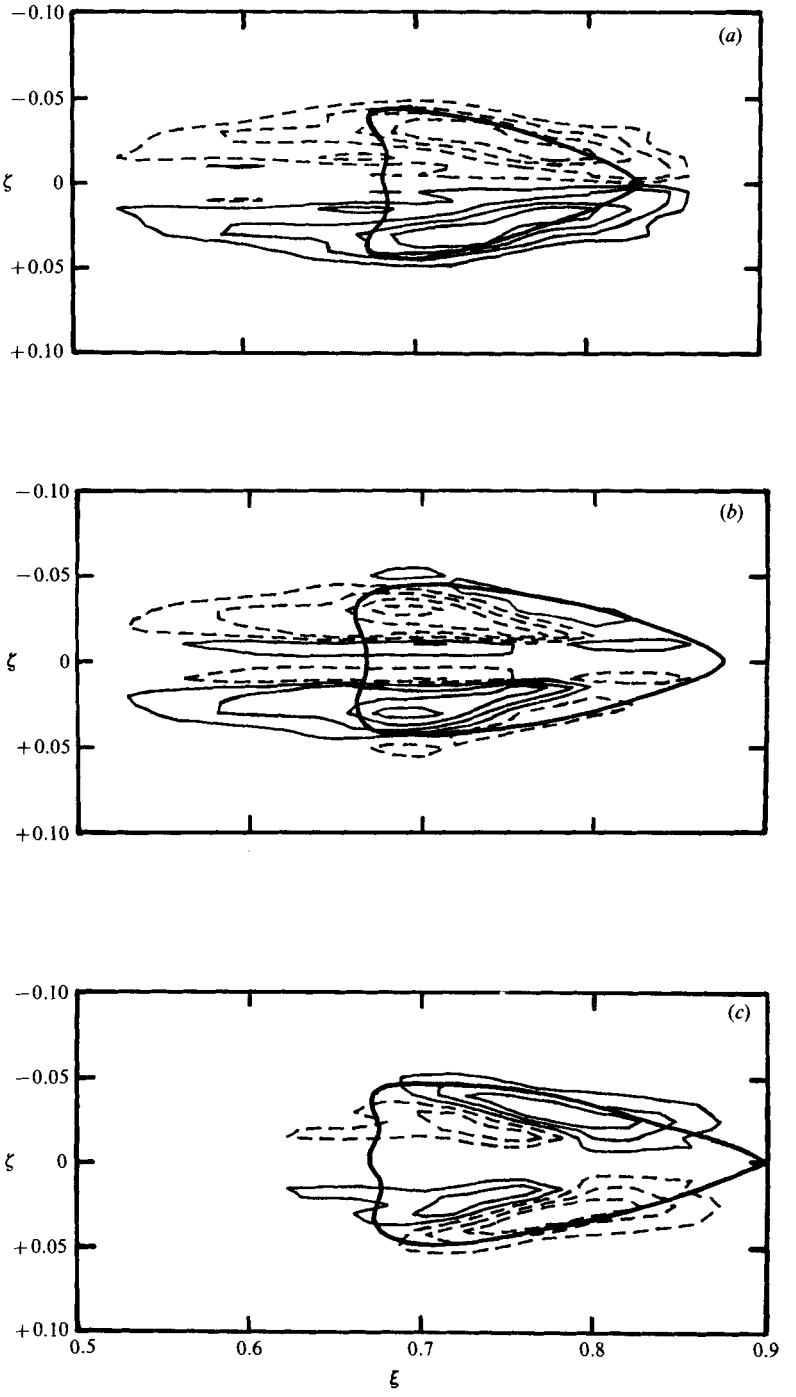

FIGURE 9. Contours of constant dimensionless vertical vorticity ω for an ensemble-averaged spot: (*a*) $y = 0.5$ mm; (*b*) 2.5 mm; (*c*) 5 mm. ——, $\omega > 0$ (2, 6, 10, 14); – – – –, $\omega < 0$ (−2, −6, −10, −14); ——, laminar–turbulent interface.

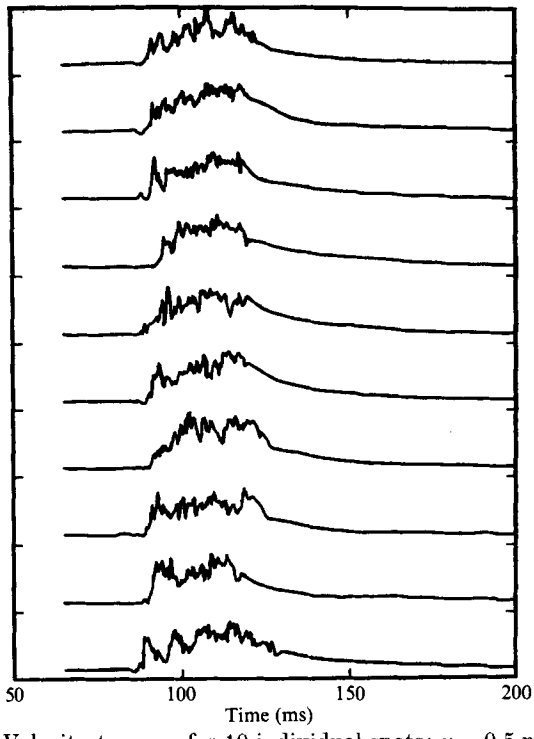

FIGURE 10. Velocity traces u for 10 individual spots; $y = 0.5$ mm, $z = 4$ mm.

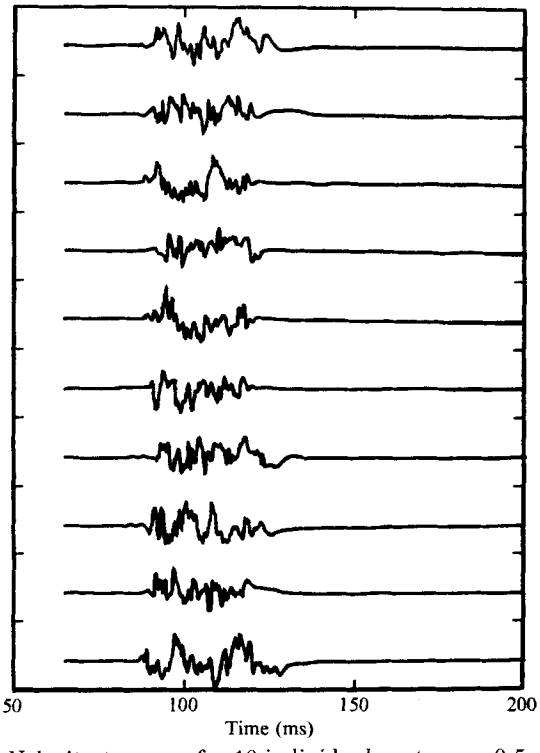

FIGURE 11. Velocity traces w for 10 individual spots; $y = 0.5$ mm, $z = 4$ mm.

and the vorticity $\Omega = \partial U/\partial z - \partial W/\partial x$ becomes

$$\omega(\xi, \zeta) = \frac{\partial}{\partial \zeta}\left(\frac{U}{U_\infty}\right) - \frac{\partial}{\partial \xi}\left(\frac{W}{U_\infty}\right).$$

This vorticity ω has been defined at constant $\eta' = y/\delta^*$, where δ^* is the turbulent boundary-layer thickness. In order to reduce numerical errors due to the computation of the velocity gradients, the data were oversampled in time and somewhat in space (z). Then, before transformation to conical coordinates, high-frequency noise fluctuations on both $\langle U \rangle$ and $\langle W \rangle$ were removed by careful smoothing. Finally, the transformed velocity field was interpolated from a non-uniform grid to a rectangular grid in ξ and ζ. Figure 9 shows contours of constant ω for an ensemble-averaged spot in horizontal planes at $y = 0.5$, 2.5 and 5 mm from the plate. The laminar–turbulent interface has been marked at each height. In a top view, positive contours correspond to a counterclockwise rotation and negative contours to a clockwise rotation. The sign and location of the counterclockwise (for $\xi > 0$) rotating feature is consistent with the representation of the globally ensemble-averaged spot as a large horseshoe vortex or vortex tube as suggested by Coles & Barker (1975). Sufficiently far away from the plate, lobes of opposite vorticity appear on both sides of the original lobes. They might represent counter-rotating lumps of outer fluid added by destabilization of the unstable laminar boundary layer in the vicinity of the turbulent spot, as suggested by Gad-El-Hak *et al.* (1981). Interpretations are difficult because the global ensemble average (on the scale of the whole spot) differs fundamentally from the instantaneous description sought using flow visualization to investigate the flow structure.

5. Ensemble averaging of localized substructures

While global ensemble mean-velocity and wall-pressure fields in turbulent spots provide information on the general shape of the spots and an overall entrainment picture, the large size of turbulent spots compared with the laminar boundary-layer thickness makes it improbable that a turbulent spot can be represented as a single large structure. Visual observations (Matsui 1980; Gad-El-Hak *et al.* 1981) support this conjecture. Another representation, using a local ensemble averaging, is needed to resolve spot substructure. The averaging must identify and align the substructures, while taking into account the fact, illustrated in figures 10 and 11, that individual spots arrive at the measuring station at different times, and are of different lengths and strengths.

After examining numerous records, Wygnanski (1981*b*) proposed and implemented a relatively simple method to identify coherent substructures in turbulent spots. Individual traces of the longitudinal velocity were digitally low-pass filtered at 350 Hz using a recursive two-pole filter to remove the effect of small-scale turbulent fluctuations. The filter was applied forward and then backward in order to eliminate any phase shift at the lowest frequencies. Then the local minima (which can perhaps be associated with vortex structures) with an amplitude greater than a fixed threshold level were detected. For each of the 250 records, the number of minima and their arrival time were stored. The choice of both filtering frequency and threshold introduce elements of subjectivity. The consistency of the choice of the filtering frequency was checked afterwards by examining the size of the minima and the separation between them.

For the present data, at each y-location the most-probable number of velocity

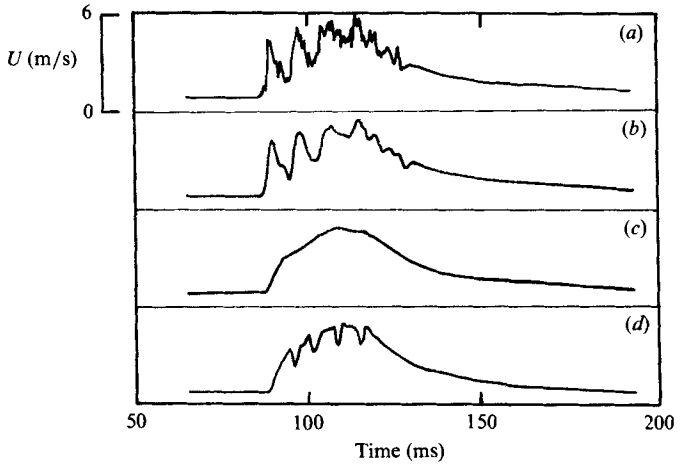

FIGURE 12. Comparison betweeen (*a*) individual, (*b*) filtered, (*c*) ensemble-averaged and (*d*) statistically most-probable spots at $y = 0.5$ mm, $z = 4$ mm.

minima and the preferred arrival time of these minima were computed. Results are in good agreement with Wygnanski (1981*b*). A simple global ensemble average of the selected turbulent spots does not give a very sharp representation of a most-probable spot because the jitter in arrival time around the preferred (i.e. mean) arrival times of the minima smooths out some of these minima. Only those spots for which the arrival times of their velocity minima fall within ± 3 ms of their respective preferred arrival time were further selected. This procedure reduces the subjectivity of the choice of the threshold level. The percentage of spots finally selected was 20–30 % of the total number. This percentage is 5 % lower than the number reported by Wygnanski (1981*b*) because of the tighter selection criterion based on the arrival times of velocity minima. The final ensemble average was performed by successively aligning the unfiltered selected spots on the most probable arrival time of the leading edge and each velocity minimum. The various averages were then patched together to reconstruct the 'statistically most-probable' spot. Figure 12 compares an individual spot with the globally ensemble-averaged and most-probable spots.

In the central region of the spot, four to five eddies were identified, with this number decreasing near the vertical and transverse boundaries of the spot. The selection was made by looking at the longitudinal velocity, but the same velocity minima can be observed in the locally averaged transversal velocity. The average separation between eddies is 6–7 ms, compared with Wygnanski's result of 8 ms under similar experimental conditions ($U_\infty = 6$ m/s, $x_s = 375$ mm, $x = 975$ mm).

6. Velocity and vorticity of the most-probable spot

Figures 13 and 14 show vertical cuts of velocity perturbation contours for a globally ensemble-averaged spot for y-values less than the laminar boundary-layer thickness δ_ℓ. For comparison purposes, the heights of 0.5, 2.5 and 5 mm used in figures 7–10 are equal to 0.075 δ_ℓ, 0.376 δ_ℓ and 0.75 δ_ℓ respectively. The ensemble-averaged results are consistent with earlier results (WSF; Antonia *et al.* 1981) and the representation of the ensemble-averaged spot as a single large structure. By comparison, the statistically most-probable spot presents a much richer structure (figures 15–17) in

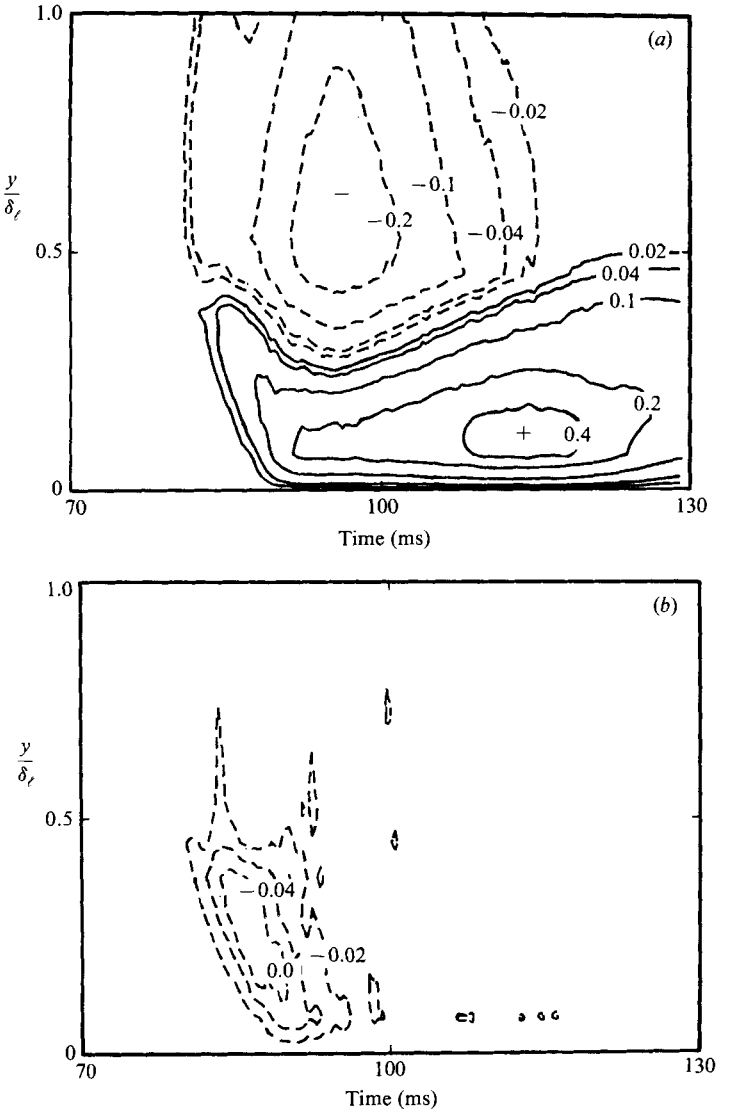

FIGURE 13. Elevation view of constant velocity-perturbation contours near the wall at $z = -1$ mm for an ensemble-averaged spot: (*a*) $(\langle U\rangle - U_\ell)/U_\infty$; (*b*) $\langle W\rangle/U_\infty$.

its central region. U_S and W_S refer respectively to the longitudinal and transverse velocities of a statistically most-probable spot. At least four eddies are clearly identified for the longitudinal velocity U_S. The number of substructures deduced by the present objective hot-wire technique is thus consistent with the four or five large vortices observed by Matsui (1980) in both artificially generated (Matsui's figure 2) and natural (Matsui's figure 5) transition spots. The same structures are barely visible in the transverse velocity because of the small random fluctuations still remaining after averaging. A much larger number of realizations would be needed to eliminate the small-scale fluctuations. The large structures seem to be associated with narrow vertical W_S extrema. Near the wingtip of the spot (figure 18), only two eddies can be identified. These may be considered as continuations of the structures observed for smaller z, as Matsui's flow visualizations (his figures 1 and 3) and the present data show that the vortical regions have a swept-back structure.

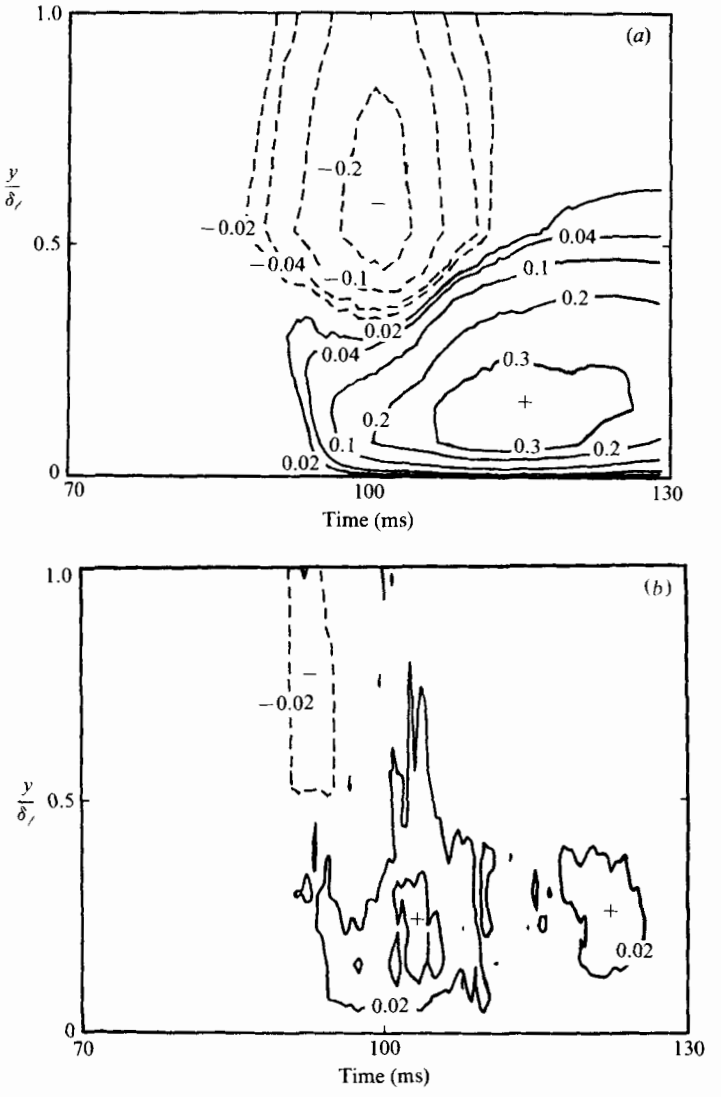

FIGURE 14. Elevation view of constant velocity-perturbation contours near the wall at $z = 22$ mm for an ensemble-averaged spot: (*a*) $(\langle U\rangle - U_l)/U_\infty$; (*b*) $\langle W\rangle/U_\infty$.

The vorticity contours for the most-probable spot are presented in figure 18 for horizontal planes at the same heights above the plate as for the ensemble-averaged data in figure 9. Near the wall (0.5 mm), several rows of four vorticity extrema are observed. All the extrema on a given row are located along lines ζ = constant, which means that, in physical space, they are arranged along rays originating from the spot virtual origin. Wider vorticity extrema of opposite sign extend from the side of the spot to its wingtips. They might be the signature of external laminar fluid which has just been destabilized by a breakdown of the laminar boundary-layer region in the vicinity of the spot wings. At the rear of the spot, where the flow is no longer turbulent and stable (the laminar profiles are very full) all the vorticity contours are elongated. According to the visual observations of Matsui (1980) and Gad-El-Hak *et al.* (1981), further downstream these long structures would break up into smaller hairpin vortices. In particular, Matsui (1980) noted that, when the spots were viewed in

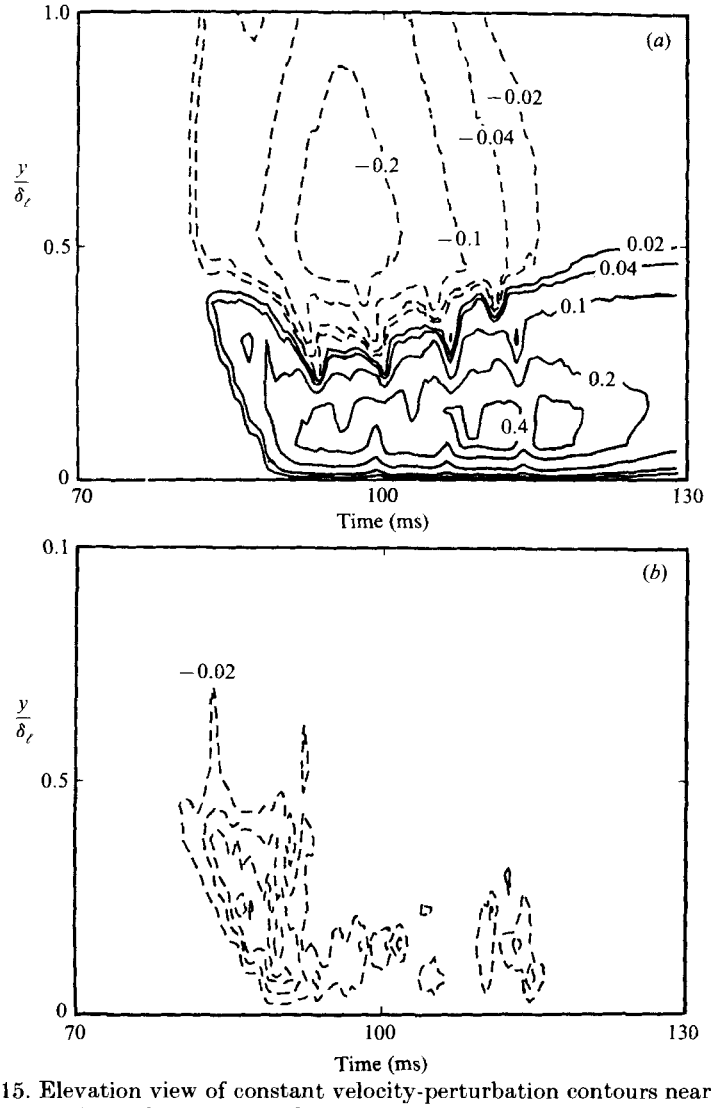

FIGURE 15. Elevation view of constant velocity-perturbation contours near the wall at $z = -1$ mm for a most-probable spot: (*a*) $(U_S - U_\ell)/U_\infty$; (*b*) W_S/U_∞.

planform, smaller-scale structures were generated on the larger-scale vortical regions, remarking, e.g., 'two horseshoe vortices smaller than the original one...originated from a leg of the original horseshoe vortex'. If these smaller structures were sufficiently phase-locked with the larger structure then the vertical component of their vorticity might be detectable in the planform vertical vorticity averages of the 'most-probable spot'. At $y = 2.5$ mm a new row of vorticity extrema of opposite sign appear on each side of the centreline and some new extrema have been created along the side of the spot where destabilization is thought to occur. The large vorticity *minimum* and the *maximum* at the rear of the spot persist but are reduced in amplitude. The measured vorticity contours at $y = 5$ mm can be compared with Leonard's (1981) vortex-simulation calculation. Leonard finds that at $y/\delta^* = 0.66$ the vertical vorticity field consists of three cell-like regions of alternating vorticity elongated along the direction of the flow. Each cell-like structure contains smaller

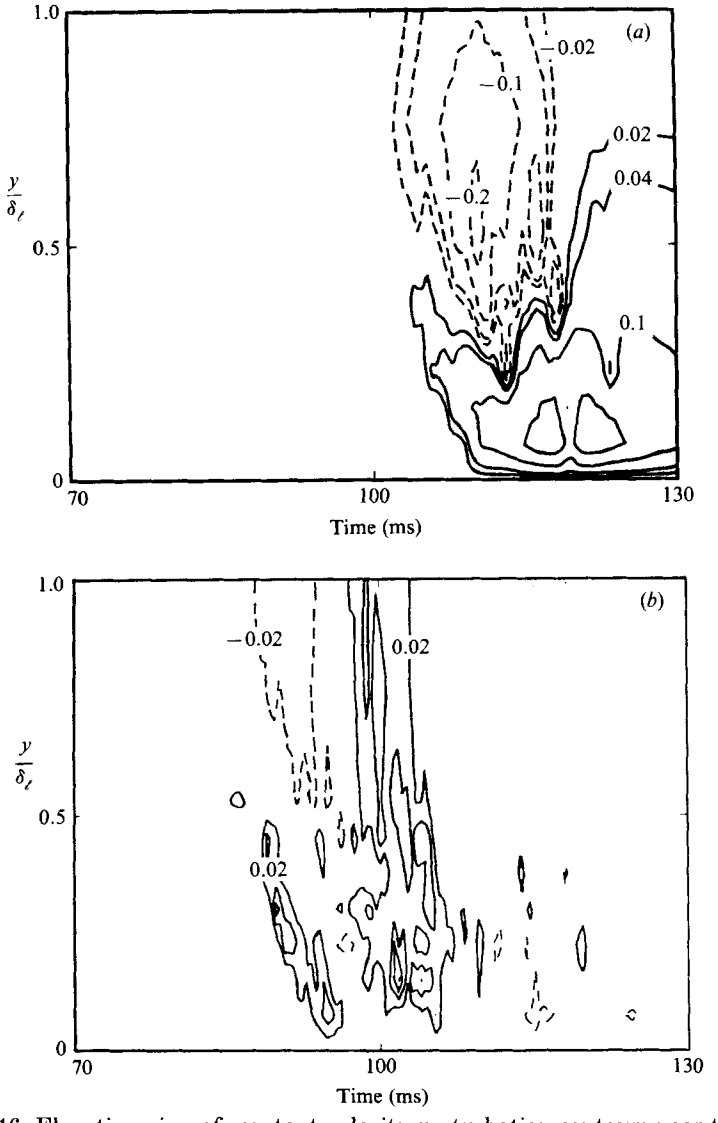

FIGURE 16. Elevation view of constant velocity-perturbation contours near the wall at $z = 22$ mm for a most-probable spot: (*a*) $(U_S - U_\ell)/U_\infty$; (*b*) W_S/U_∞.

cells distributed along the longitudinal axis x. The numerical results are in good qualitative agreement with the present measurements in terms of the vorticity sign and the shape of the cells. Both representations show that turbulent flows have a strong transversal coherence as well as a longitudinal coherence.

The vortex-like motions of the spot substructures can be observed more directly by looking at the space–time (z, t)-distribution of the horizontal velocity field without resorting to the assumption of conical similarity. Figure 19(a, b, c) presents the perturbation velocity vectors in the three horizontal planes used previously ($y = 0.5$, 2.5 and 5 mm). The solid lines in these figures mark the laminar–turbulent interface of the spots as defined by WSF. The perturbation trajectories, which can be obtained by joining the velocity vectors, lead to a pattern matching the vertical vorticity contours of figure 18. At $y = 2.5$ and 5 mm there are several rows of vortex-like eddies

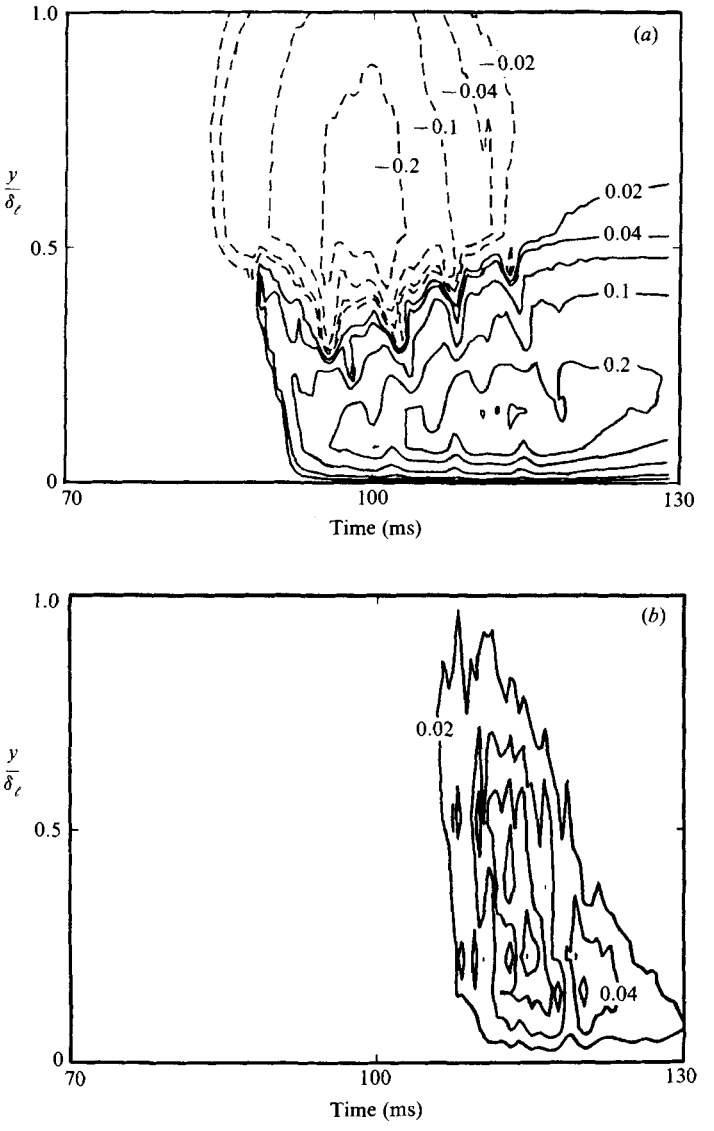

FIGURE 17. Elevation view of constant velocity-perturbation contours near the wall at $z = 43$ mm for a most-probable spot: (*a*) $(U_S - U_\ell)/U_\infty$; (*b*) W_S/U_∞.

aligned parallel to the leading laminar–turbulent interface, and near the wingtip there is a large sweptback vortex similar to the one observed by Matsui (1980). Since WSF and Mau?ner (1983) showed that the velocity of the trailing laminar–turbulent interface was $0.55U_\infty$, independent of spanwise (z) and vertical (y) coordinates, it is apparent, at least for $y = 2.5$ and 5 mm, that a large number of fluid particles are engulfed into the spot through the trailing edge. In both figures 19(*b*) and (*c*) the laminar velocities which were subtracted from the total velocity are $0.58U_\infty$ and $0.93U_\infty$ respectively. It is not possible to compute the net entrainment rate through the interface because the vertical velocity v is not known.

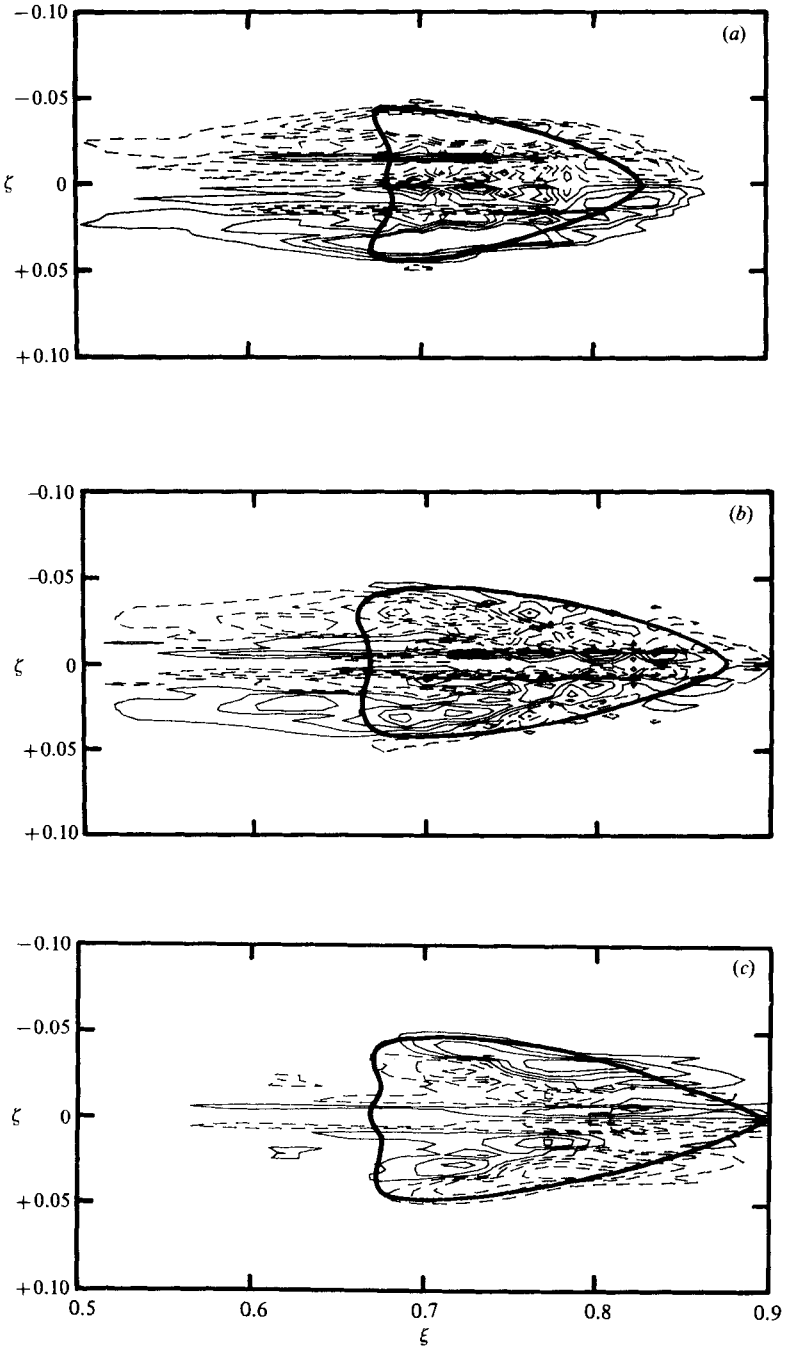

FIGURE 18. Contour of constant vertical dimensionless vorticity ω for most-probable spot in similarity coordinates: (*a*) $y = 0.5$ mm; (*b*) 2.5 mm; (*c*) 5 mm. ——, $\omega > 0$ (2, 6, 10, 14); – – – –, $\omega < 0$ (−2, −6, −10, −14); ——, laminar–turbulent interface.

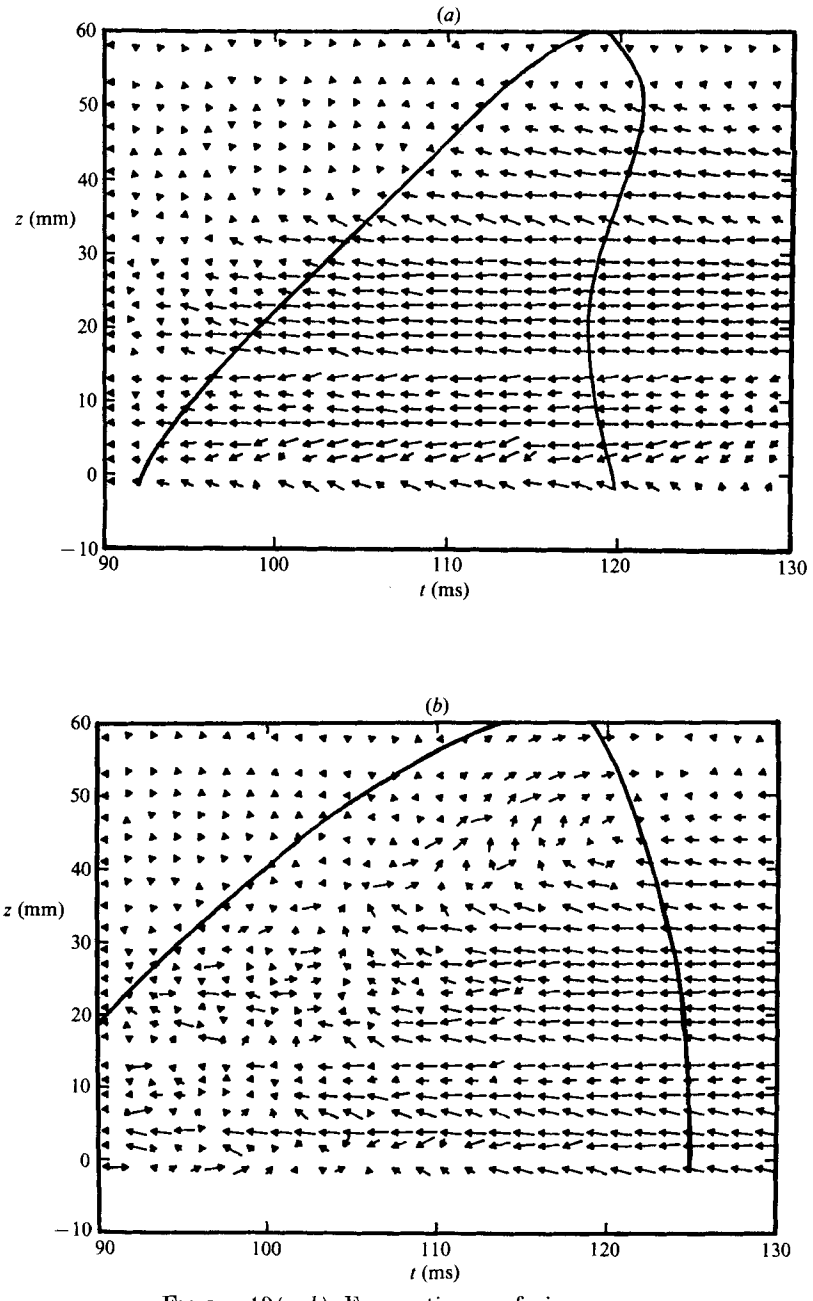

FIGURE 19(*a*, *b*). For caption see facing page.

7. Conclusions

Longitudinal and transversal velocity measured simultaneously at various heights and off-axis locations describe the globally ensemble-averaged spot as a single large horseshoe vortex tube. This result inadequately describes the structure of turbulent spots. Perry *et al.* (1981) suggest that 'what is really needed is an experiment in which identical spots can be produced by periodic disturbances, thus enabling them to be frozen. Phase-averaged measurements with anemometers could then be utilized to

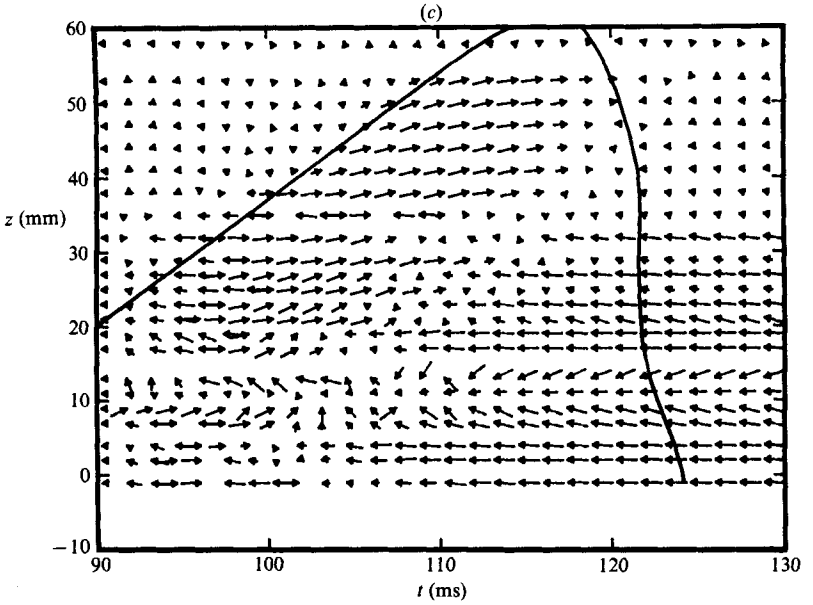

FIGURE 19. Perturbation-velocity diagrams for a most-probable spot at: (*a*) $y = 0.5$ mm; (*b*) 2.5 mm; (*c*) 5 mm.

obtain the detailed motions.' Selecting only spots with a certain fixed number of substructures is one operational means of producing 'identical' spots. Here a selective (or local) averaging technique was used to reconstruct a statistically most-probable spot to obtain a more physically accurate representation of the structure of turbulent spots.

Coherent rows of four eddies were identified, but the mechanisms through which external fluid is entrained into the spots are not fully described by this new representation. The time separation between eddies is 6–7 ms for a free-stream velocity $U_\infty = 8.6$ m/s. Newly entrained fluid seems to be associated with vorticity extrema of sign opposite to the principal vorticity of the fluid initially in the turbulent spots. Measurements of u and w at several downstream stations would be useful in order to see how those vorticity cells evolve as the turbulent spot grows. Unfortunately, the available flow-visualization results are not well suited for comparison with this data, as the planform visualizations have not been designed to emphasize the vertical vorticity. To visualize the vertical vorticity component effectively, one would ideally need to introduce the marker fluid in a vertical sheet of small z-extent and make the observations viewing the (x, z)-plane from above or below. Available flow visualizations (e.g. those of Matsui 1980; Gad-El-Hak *et al.* 1981; Perry *et al.* 1981) have observed the planform by introducing the marker in a horizontal plane, or have not observed the flow in planform when the marker was introduced in a narrow vertical strip (e.g. the hydrogen-bubble visualizations in Matsui's figure 2). While the planform visualizations generally agree on the presence of smaller horseshoe or Λ-shaped vortices, Matsui remarks that 'many kinds of vortices, that is, hairpin, ring, wavy and winding, are observed'. The small-scale vertical vorticity regions observed in figures 18 and 19 are compatible with the visualization results if they are interpreted as arising from horizontal cuts through the inclined primary or smaller-scale vortical structures. At $y = 2.5$ and 5 mm the prominent sweptback regions in which the sign of the vorticity does not change are consistent with Matsui's pictures showing several

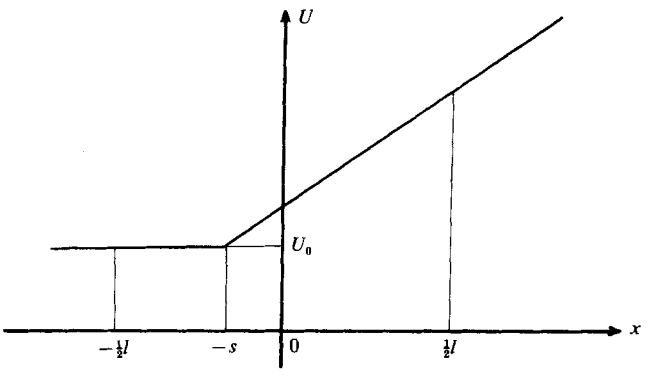

FIGURE 20. Probe resolution in a linear velocity gradient.

sweptback regions of wavy vortices. The number of local maxima or minima is of the same order of magnitude as the number of small structures seen in visualizations, but no definite conclusions about their possible vortex geometry can be drawn from our data. We can only conclude that the present attempt to employ the 'most-probable spot' to identify smaller-scale substructures suggests considerable phase coherence between the structure of the 'most-probable spot' and vortical motions on the next-smaller scale. Future investigations might be more suitable for comparison with flow visualizations if they employed selective averaging of the longitudinal or lateral vorticity components, rather than the vertical.

Appendix. Estimate of velocity errors due to probe resolution

Let us consider the case of a linear velocity gradient that occurs over a distance greater than the wire sensing length l in that direction. For simplicity, the wire is assumed to have a uniform temperature along its length. A parabolic temperature distribution would effectively reduce the sensing length of the wire. In the coordinates of figure 20 the velocity that would be measured by a infinitely short wire at $x = 0$ is

$$U_{\text{true}} = U_0 + \left(\frac{\partial U}{\partial x}\right) s.$$

The actual measured velocity, for a wire with length l whose midpoint is at $x = 0$, is

$$\begin{aligned} U_{\text{meas}} &= \frac{1}{l}\int_{-\frac{1}{2}l}^{\frac{1}{2}l} U\,\mathrm{d}x \\ &= U_{\text{true}} + U_{\text{error}}. \end{aligned}$$

By separating the integral in two parts we obtain

$$\begin{aligned} U_{\text{meas}} &= \frac{1}{l}\left[U_0(\tfrac{1}{2}l - s) + \int_{-s}^{\frac{1}{2}l}\left(U_0 + \left(\frac{\partial U}{\partial x}\right)(x+s)\right)\mathrm{d}x\right] \\ &= U_0 + \frac{1}{8}\left(\frac{\partial U}{\partial x}\right) l + \frac{1}{2l}\left(\frac{\partial U}{\partial x}\right) s^2 + \frac{s}{2}\left(\frac{\partial U}{\partial x}\right). \end{aligned}$$

Therefore the error velocity is

$$U_{\text{error}} = \frac{1}{8}\left(\frac{\partial U}{\partial x}\right) l + \frac{1}{2l}\left(\frac{\partial U}{\partial x}\right) s^2 - \frac{1}{2}\left(\frac{\partial U}{\partial x}\right) s.$$

The error is maximum for $s = 0$ and equal to

$$U_{\text{error}} = \frac{1}{8}\left(\frac{\partial U}{\partial x}\right) l.$$

If $s \geqslant \frac{1}{2}l$ there is no error in the velocity due to probe resolution in a linear velocity gradient.

REFERENCES

ANTONIA, R. A., CHAMBERS, A. J., SOKOLOV, M. & VAN ATTA, C. W. 1981 Simultaneous temperature and velocity measurements in the plane of symmetry of a transitional turbulent spot. *J. Fluid Mech.* **108**, 317–393.

CANTWELL, B. J., COLES, D. & DIMOTAKIS, P. 1978 Structure and entrainment in the plane of symmetry of a turbulent spot. *J. Fluid Mech.* **87**, 641–672.

COLES, D. & BARKER, S. 1975 Some remarks on a synthetic turbulent boundary layer. In *Turbulent Mixing in Nonreactive and Reactive Flows* (ed. S. M. B. Murthy). Plenum.

EMMONS, H. W. 1951 The laminar–turbulent transition in a boundary layer. Part I. *J. Aero. Sci.* **18**, 490.

GAD-EL-HAK, M., BLACKWELDER, R. F. & RILEY, J. J. 1981 On the growth of turbulent regions in laminar boundary layers. *J. Fluid Mech.* **110**, 73–96.

HEAD, M. R. & BANDYOPADHYAY, P. 1981 New aspects of turbulent boundary-layer structure. *J. Fluid Mech.* **107**, 297–338.

ITSWEIRE, E. C. 1983 An investigation of the coherent structures associated with a turbulent spot in a laminar boundary layer. Ph.D. thesis, University of California, San Diego.

ITSWEIRE, E. C. & VAN ATTA, C. W. 1983 The effect of different similarity growth transformations on ensemble mean particle paths in turbulent spots. *J. de Phys. Lett.* **44**, 917–923.

LEONARD, A. 1980 Vortex simulation of three-dimensional spotlike disturbances in a laminar boundary layer. In *Turbulent Shear Flows II* (ed. L. J. S. Bradbury *et al.*), pp. 67–77. Springer.

LEONARD, A. 1981 Turbulent structures in wall-bounded shear flow observed via three-dimensional numerical simulations. In *The Role of Coherent Structures in Modelling Turbulence and Mixing* (ed. J. Jimenez). Lecture Notes in Physics, vol. 136, pp. 119–145. Springer.

MATSUI, T. 1980 Visualization of turbulent spots in the boundary layer along a flat plate in a water flow. In *Proc. IUTAM Symp. on Laminar–Turbulent Transition, Stuttgart* (ed. R. Eppler & H. Fasel), pp. 288–296. Springer.

MAUTNER, T. S. 1983 Investigation of the wall pressure, wall shear stress and velocity fields associated with a turbulent spot in a laminar boundary layer. Ph.D. thesis, University of California, San Diego.

MAUTNER, T. S. & VAN ATTA, C. W. 1982 An experimental study of the wall-pressure field associated with a turbulent spot in a laminar boundary layer. *J. Fluid Mech.* **118**, 59–77.

PERRY, A. E. & CHONG. M. S. 1982 On the mechanism of wall turbulence. *J. Fluid Mech.* **119**, 173–217.

PERRY, A. E., LIM, T. T. & TEH, E. W. 1981 A visual study of turbulent spots. *J. Fluid Mech.* **104**, 387–405.

SCHLICHTING, H. 1956 *Boundary Layer Theory*. McGraw-Hill.

SCHUBAUER, G. B. & KLEBANOFF, P. S. 1956 Contributions on the mechanisms of boundary layer transition. *NACA Rep.* 1289.

VAN ATTA, C. W. & HELLAND, K. N. 1980 Exploratory temperature-tagging measurements of turbulent spots in a heated laminar boundary layer. *J. Fluid Mech.* **100**, 243–255.

WYGNANSKI, I. 1981*a* The effect of Reynolds number and pressure gradient on the transitional spot in a laminar boundary layer. In *The Role of Coherent Structures in Modelling Turbulence and Mixing* (ed. J. Jimenez). Lecture Notes in Physics, vol. 136, pp. 304–332. Springer.

WYGNANSKI, I. 1981*b* On turbulent spots. In *Proc. 7th Symp. on Turbulence, University of Missouri–Rolla, Sept. 1981* (ed. Patterson & Zakin), pp. 390–400.

WYGNANSKI, I., HARITONIDIS, J. & KAPLAN, R. E. 1979 On a Tollmien–Schlichting wave packet produced by a turbulent spot. *J. Fluid Mech.* **92**, 505–528.

WYGNANSKI, I., SOKOLOV, M. & FRIEDMAN, D. 1976 On the turbulent 'spot' in a laminar boundary layer. *J. Fluid Mech.* **78**, 785–819.

WYGNANSKI, I., ZILBERMAN, M. & HARITONIDIS, J. H. 1982 On the spreading of a turbulent spot in the absence of a pressure gradient. *J. Fluid Mech.* **123**, 69–90.

ZILBERMAN, M. 1981 On the interaction of transitional spots and generation of a synthetic turbulent boundary layer. Ph.D. thesis, Tel-Aviv University.